

A discontinuous Galerkin based multiscale method for compressible multiphase flow

S. Fechter*, F. Jaegle*, M. Boger*, C. Zeiler**, C.-D. Munz* and C. Rohde**
Corresponding author: stefan.fechter@iag.uni-stuttgart.de

* Inst. of Aerodynamics and Gas Dynamics, Univ. of Stuttgart, Germany;

** Inst. of Applied Analysis and Numerical Simulation, Univ. of Stuttgart, Germany.

Abstract: In this study, a numerical method for the simulation of compressible two-phase flows is presented. The multiscale approach consists of several components: a discontinuous Galerkin (DG) solver for the macroscopic scales of the flow, a micro-scale solver at the interface, a level-set interface tracking formalism as well as an adaptive mesh refinement near the phase interface. The method is demonstrated for a droplet at equilibrium, a moving droplet as well as a shock-droplet interaction. Thereby, the full Navier-Stokes equations are used to describe the problem. The present approach for the multi-phase coupling is not suitable for phase change calculations as the present micro-scale solver is not capable to resolve this. The chosen approach includes the sharp resolution of the phase interface as well as surface tension.

Keywords: DNS, Discontinuous Galerkin, Multiscale, Compressible multiphase flow.

1 Introduction

In many technical applications, multiphase flows meet conditions such as high pressures and/or high velocities that prohibit the popular assumption of incompressibility. The most important examples are fuel injection systems of aeronautical, automotive and rocket engines. The numerical simulation of compressible multiphase flow presents additional difficulties to the numerical approach, compared to the incompressible treatment that is most often found in two-phase numerical solvers in practical use today.

Two elements of the numerical algorithm are crucial: A method that allows to define the geometry, the temporal evolution of the interface between the two phases (in this study, we employ a level-set method) as well as a numerical strategy to treat the discontinuous nature of the interface together with the related physical processes such as surface tension or phase change. In the compressible case this includes different equations of state (EOS) on both sides of the phase interface. In principle, the interface region can be approximated by a smooth transition that can be handled by the numerical scheme (diffuse interface approach). As an alternative, we use a sharp interface multiscale approach, there the numerical scheme only resolves the macroscopic scales of the flow and allows discontinuous states at the interface position, where jump conditions have to be provided by an additional solver for the micro-scale. Many micro-scale solvers are conceivable, in the present study, we rely on Riemann-type solvers [1, 2]. The approach is suitable for general EOS. A well-known method of this type is the so-called ghost fluid formalism of Fedkiw et al. [3], developed for finite volume schemes, where fictitious fluid states are introduced near the interface, similar to the well-known concept of ghost-cells at boundaries. This method has been continuously refined, e.g. by Liu et al. [4], Hu et al. [2] and Ferrari et al. [5].

In this paper we present a sharp interface method based on a discontinuous Galerkin spectral element method (DGSEM) that allows for a high order of accuracy as well as efficient calculations. The discontinuous Galerkin (DG) formulation allows for discontinuities at the element interfaces, which simplifies the implementation of the sharp interface approach as only numerical fluxes have to be adapted. A further advantage is that it is straightforward to include the effects of surface tension into the algorithm as only the micro-scale

solver has to be updated. The high-order approximation of the level-set allows for curvature calculation at the phase boundary. This information is needed to include the effect of surface tension in the algorithm. The native DG implementation is only capable to resolve the phase boundary at the nearest cell boundary. This is related to the fact that solely at element boundaries discontinuous states are permitted due to the use of Riemann solvers. Typically, such discontinuities occur at phase boundaries as e.g. a density jump is present. The DG cells are comparatively large due to the in-cell resolution resulting in a coarse numerical approximation of the phase boundary. One approach to improve the phase boundary resolution is to use an Adaptive Mesh Refinement (AMR) at phase boundaries. In this case, one DG cell is replaced by multiple finite-volume cells allowing for an improved resolution of the numerical phase boundary as in the finite-volume context discontinuities between each DOF are allowed. This approach shows promising results for future investigations combining the high-order resolution of the DG scheme as well as a fine resolution of the phase boundary. The level-set variable is always treated with the high-order DG method to take advantage of the low dispersion and dissipation properties.

The paper is organized as follows: in the first section, the numerical method is described followed by an outline of the information transfer between macro- and micro-scale model. In the next section first results of droplet simulations are presented and in the last section a summary and conclusion is drawn.

2 The numerical method

In this paper we present a novel multi-scale method for the calculation of compressible multiphase flows. To be able to include interface phenomena such as surface tension into the algorithm, a heterogeneous multiscale method (HMM) is chosen. We consider the compressible Navier-Stokes equations as macro-scale model. The solution for the macro-scale model is provided by a discontinuous Galerkin spectral element method (DGSEM) based explicit solver as developed by Kopriva [6]. The micro-scale solver may be based on different concepts such as Riemann solvers or well-resolved 1D simulations. In the present study, we use a HLLC-type Riemann solver as developed by Hu et al. [2]. The effect of the Young-Laplace equation

$$(\rho(\mathbf{v} \cdot \mathbf{n} - s)\mathbf{v} + p(\rho)\mathbf{n}) = (d - 1)\sigma\kappa\mathbf{n}, \quad (1)$$

describing the surface tension at the phase boundary enters the HMM as micro-scale model. With κ we denote the mean curvature of the level-set approximation associated with the orientation of the mean normal \mathbf{n} . The surface tension coefficient σ is assumed to be constant and positive. This problem can be handled in a generalized Riemann problem with non-homogeneous jump conditions. An accurate polynomial description of the phase interface is provided by the level-set dividing the cells such that a cell is either in the gaseous or in the liquid phase. The physical interface is described by the root of the level-set polynomial while the computational interface is described by the surface dividing the cells that are predominately occupied by either the gas or the liquid phase.

The macro-scale solver is independent of the used equation of state (EOS). Different EOS can be applied for the different phases as a level-set based phase tracking algorithm is used. In the present case we use different EOS for the liquid as well as the vapor phase of the fluid. For the gaseous part we applied the ideal gas law whereas we use the weakly compressible Tait EOS to model the liquid phase. Note that the micro-scale solver applied at the phase boundary is generally not independent of the EOS formulation. Multiphase Riemann solver formulations that satisfy this property for the case without phase change are available [7]. In the following we will describe the basic steps of the HMM algorithm, that is visualized in figure 1.

- Step 1: Computation of the discrete curvature at the faces of the computational interface using the level-set solution. Furthermore, the calculation of the states at the element boundaries is done.
- Step 2: Solution of the Riemann problem (micro-solver) at the element boundaries. For each surface integration point at the numerical interface a generalized Riemann problem is solved that takes the local curvature into account. The initial conditions are provided by the approximate solutions for the liquid and gas phase. The solution of the micro-solver contains the phase boundary and is moving with the local normal interface speed \mathbf{s} .

For the bulk phases a standard one-phase Riemann solver is used that takes the corresponding EOS into account. Due to the large computation effort, typically approximative Riemann solvers are used.

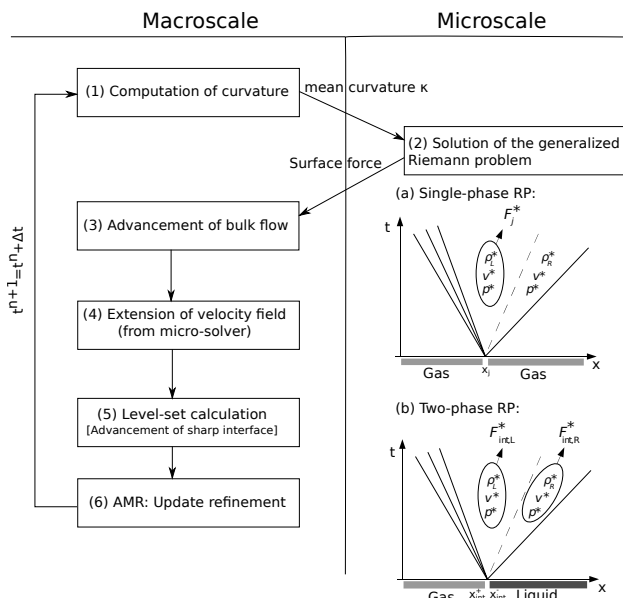


Figure 1: HMM algorithm used for the simulation of compressible multiphase flows.

- Step 3: The explicit DGSEM scheme is used to advance the bulk flow to the next time level t^{n+1} . At the computational interface the respective flux contributions for the different phases as determined in step 2 are used (ghost fluid approach).
- Step 4: The local normal interface speed s defined at the computational interface is extended to a global velocity field. This velocity field is used to advance the physical interface represented by the level-set variable.
- Step 5: The new position of level-set zero is used to determine the new physical and computational interfaces. In case the interface has moved across a grid cell, the new state is extrapolated using the adjacent grid cells.
- Step 6: In case the adaptive mesh refinement (AMR) is used, the refinement indicator is calculated. According to the indicator value a cell is refined using multiple finite-volume cells or coarsened to the DG grid. In this step a conservative interpolation/projection method is used to ensure a conservative coupling between the parts.

In the following sections the basic steps of the HMM algorithm are described in detail.

2.1 The Macro-Scale Solver: a Discontinuous Galerkin spectral element method

In this section we describe the the macro-scale solver used in Step 3 of the HMM Algorithm that is visualized in figure 1. In both cases we rely on a DGSEM. The description of the method is kept brief, for more details, we refer to [6, 8].

The key properties of the method are: the three-dimensional domain is divided into non-overlapping hexahedral elements, each mapped onto a reference cube element $E := (-1, 1)^3$ by a mapping $\mathbf{x}(\boldsymbol{\zeta})$. The equations are solved in the reference element. The weak solution vector \mathbf{U} of a general system of conservation laws of the type

$$\mathbf{U}_t + \operatorname{div} \mathbf{F}(\mathbf{U}) = \mathbf{0} \quad (2)$$

with a flux $\mathbf{F}(\mathbf{U}) = (\mathbf{F}^1(\mathbf{U}), \mathbf{F}^2(\mathbf{U}), \mathbf{F}^3(\mathbf{U}))^T$ is approximated by a tensor-product basis

$$\mathbf{U}(\boldsymbol{\zeta}) = \sum_{i,j,k=0}^N \hat{\mathbf{U}}_{ijk} \psi_{ijk}(\boldsymbol{\zeta}), \quad \psi_{ijk}(\boldsymbol{\zeta}) = l_i(\zeta^1) l_j(\zeta^2) l_k(\zeta^3), \quad (3)$$

where $l_j(\zeta)$ are 1D Lagrange polynomials of degree N defined as:

$$l_j(\zeta) = \prod_{\substack{i=0 \\ i \neq j}}^N \frac{\zeta - \zeta_i}{\zeta_j - \zeta_i}, \quad j = 0, \dots, N. \quad (4)$$

Multiplying (2) with a test function ϕ and integration by parts of the second term leads to three contributions: a volume integral of the time derivative term (a), a surface integral term (b) and a volume integral term (c), which now contains the gradient of the test function ϕ

$$\underbrace{\frac{\partial}{\partial t} \int_E \mathbf{J} \mathbf{U} \phi d\boldsymbol{\zeta}}_a + \underbrace{\int_{\partial E} (\mathbf{F}^* \cdot \mathbf{N}) \phi d\mathbf{S}}_b - \underbrace{\int_E \mathbf{F}(\mathbf{U}) \cdot \text{grad}(\phi) d\boldsymbol{\zeta}}_c = 0. \quad (5)$$

In this expression, \mathbf{J} is the Jacobian of the transformation to the reference cube element.

Volume as well as surface integrals are approximated by Gauss-Legendre or Gauss-Legendre-Lobatto quadrature. Quadrature points coincide with the interpolation points for the ansatz functions l_j . As no continuity constraint is enforced between the elements, the flux function $\mathbf{F}(\mathbf{U})$ at the cell boundaries is replaced by a numerical flux function $\mathbf{F}^*(\mathbf{U}^-, \mathbf{U}^+)$ depending on the left and right adjacent states \mathbf{U}^- and \mathbf{U}^+ . The approximation (3) is inserted into the weak form (5) and the test functions are chosen as the ansatz functions $\phi = \psi_{ijk}$. Integrals are split in coordinate directions and approximated by Gauss-Legendre (-Lobatto) quadrature, which introduces the integration weights ω_i , $i = 0, \dots, N$. As the quadrature points are the same as the interpolation points of l_j , the Lagrange property $l_j(\zeta_i) = \delta_{ij}$; $i, j = 0, \dots, N$ can be exploited. Plugging all the ansatz functions into the weak form, make use of the orthogonality of the ansatz functions and introduction of numerical integration yields the final semi-discrete form of the DGSEM scheme:

$$\begin{aligned} \left(\hat{\mathbf{U}}_{ijk} \right)_t &= -(\mathbf{J}_{ijk})^{-1} \left[- \sum_{\lambda=0}^N \frac{\omega_\lambda}{\omega_i} D_{i\lambda} \mathbf{F}_{\lambda j k}^1 - \sum_{\mu=0}^N \frac{\omega_\mu}{\omega_j} D_{j\mu} \mathbf{F}_{i \mu k}^2 - \sum_{\nu=0}^N \frac{\omega_\nu}{\omega_k} D_{k\nu} \mathbf{F}_{ij \nu}^3 \right. \\ &+ \left([\mathbf{F}^* \hat{\mathbf{s}}]_{jk}^{+\zeta^1} \frac{l_i(1)}{\omega_i} - [\mathbf{F}^* \hat{\mathbf{s}}]_{jk}^{-\zeta^1} \frac{l_i(-1)}{\omega_i} \right) + \left([\mathbf{F}^* \hat{\mathbf{s}}]_{ik}^{+\zeta^2} \frac{l_j(1)}{\omega_j} - [\mathbf{F}^* \hat{\mathbf{s}}]_{ik}^{-\zeta^2} \frac{l_j(-1)}{\omega_j} \right) \\ &\left. + \left([\mathbf{F}^* \hat{\mathbf{s}}]_{ij}^{+\zeta^3} \frac{l_k(1)}{\omega_k} - [\mathbf{F}^* \hat{\mathbf{s}}]_{ij}^{-\zeta^3} \frac{l_k(-1)}{\omega_k} \right) \right]. \end{aligned}$$

The numerical fluxes \mathbf{F}^* are evaluated at the reference element faces in each coordinate direction. These terms are denoted by $\llbracket \cdot \rrbracket^{-\zeta^1}$ and $\llbracket \cdot \rrbracket^{+\zeta^1}$ for the left and right face in ζ^1 -direction and analogously for ζ^2 and ζ^3 . With $D_{ij} = dl_j(\zeta)/d\zeta|_{\zeta=\zeta_i}$ a differentiation matrix is denoted, which is needed for the evaluation of the volume integral. The numerical integration weights for the Gaussian integration are symbolized with ω . Time integration relies on an explicit third-order Runge-Kutta scheme.

2.2 The Discontinuous Galerkin spectral element method for the 3D level-set transport

The HMM approach used in this study relies on accurate geometrical information (position, curvature) of the phase boundary, which necessitates a suitable interface tracking formalism. To obtain this information we use a level-set formulation: an additional function Φ is initialized as a signed distance function with respect to the interface. The level-set function is then advected by a velocity field \mathbf{s} that is either determined from

the micro-scale solver or from the fluid velocity. The level-set advection equation reads:

$$\frac{\partial \Phi}{\partial t} + \mathbf{s} \cdot \text{grad}(\Phi) = 0 \text{ in } \Omega \times (0, T) . \quad (6)$$

Of course, this is only a conservation law as long as $\text{div}(\mathbf{s}) = 0$, which will not hold in our case as in the compressible case the divergence of the velocity is not equal to zero. To discretize (6) also with the DGSEM scheme, equation (6) is re-cast as a conservation law with an additional right-hand-side containing the divergence of the level-set advection speed \mathbf{s} :

$$\frac{\partial \Phi}{\partial t} + \text{div}(\mathbf{s}\Phi) = \Phi \text{div}(\mathbf{s}) . \quad (7)$$

Note that the divergence term can be readily obtained in the DGSEM by evaluating the necessary derivatives of the high-order ansatz polynomials.

The level-set advection speed \mathbf{s} may be chosen equal to the fluid velocity in the absence of phase transition. In a more general framework, a smooth artificial velocity field that locally coincides with the normal propagation speed of the interface at the level-set zero has to be generated. More information about the reconstruction of the advection velocity field can be found in Jaegle et al. [9].

Upon initialization, the level-set is calculated as a signed distance function using an analytic sphere geometry and in the next step cropped using a maximum and minimum level-set limit. A sine transfer function is applied in the cropping process that retains the level-set gradient around level-set zero and provides a smooth transition to the cropped level-set value. This approach avoids numerical difficulties related to a sharp cropping and is numerically beneficial.

2.3 Reinitialization of the level-set variable

In order to keep the level-set function a signed distance function, a reinitialization step has to be introduced. Due to the low dissipation and dispersion properties of the DGSEM scheme, the reinitialization procedure is used infrequently. This is essential in case colliding or advecting bubbles are existing as the desired condition $\text{div}(\Phi) = 1$ next to level-set zero can not be guaranteed for all times. The reinitialization procedure as introduced by Sussman et al. [10] can be written for the three-dimensional case in the following equation

$$\Phi_t = S(\Phi_0) \left(1 - \sqrt{\Phi_x^2 + \Phi_y^2 + \Phi_z^2} \right) , \quad (8)$$

$$\Phi(\mathbf{x}, 0) = \Phi_0(\mathbf{x}) , \quad (9)$$

where S represents a numerical sign function. This formulation avoids the explicit search for the root of the level-set function and the reset of the level-set function close to the phase front, which requires $O(N_{\text{DOF}}^3)$ operations. An additional smoothing of the numerical sign function is used in the following way

$$S_\epsilon(\Phi_0) = \frac{\Phi_0}{\sqrt{\Phi_0^2 + |\text{div}(\mathbf{s})|\epsilon}} . \quad (10)$$

In three-dimensions we chose the smoothing term ϵ according to the minimum grid length and use an additional smoothing multiplier according to the divergence of the velocity at the position. Note that the divergence information is already available as it is needed for the level-set calculation. Furthermore, the sign function is only calculated once per reinitialization process as it is only dependent on the initial conditions. Equation (8) is iterated to steady-state which is typically achieved after few iterations. The reconstructed level-set function has the property that the zero-value remains unchanged as the root of the level-set function represents the position of the physical phase boundary.

Equation (8) is of Hamilton-Jacobi type that can be discretized using a DG method proposed by Yan and Osher [11]. In this DG method the gradients of the Hamilton-Jacobi equation are approximated by additional variables. For the numerical flux functions at element boundaries, upwind and downwind fluxes are used. A Lax-Friedrichs numerical Hamiltonian is used for the calculation of the numerical fluxes. To prevent oscillations of the DG polynomial near the cropped level set value filtering is used. In this case a



Figure 2: Comparison of the phase boundary approximation for a DG scheme of order 6 using the density iso-contour of the liquid phase. **Left:** Approximation using a pure DG scheme. **Right:** Approximation using the adaptive mesh refinement at the phase boundary.

Hesthaven filter is used that locally reduces the order of the DG polynomial.

This DG method for the Hamilton-Jacobi reinitialization equation is chosen similar to the macro-scale approach as this approach retains the locality of the whole method. Similar to the DGSEM scheme, a division into volume and surface contributions is achieved. For the computation the same DG grid is used including the mapping onto the reference element. Because of that synergetic effects between the different parts of the HMM approach can be used and the method is suitable for parallel computations.

2.4 Adaptive Mesh Refinement

A difficulty arising with the present DG approach is that the numerical resolution of the phase interface is coarse and does not reflect the physical approximation of the phase boundary. This is a consequence of the comparatively large DG cells as the DG cells have an in-cell resolution. In the DG framework discontinuities are only allowed at cell interfaces which implies that the phase boundary coupling is only possible at cell boundaries. In the native DG approach the nearest grid boundary is chosen to resolve the phase boundary. Especially for higher orders, the phase boundary resolution can get really coarse and does not reflect the real position of the phase boundary. Thus, the native approach is limited to medium-order and the advantages of high-order DG methods can not be exploited to the full extent. It is especially advisable to use high order approximations for the level-set transport as the second derivative (curvature) is needed for the surface tension modeling. Furthermore, high-order schemes have considerably lower dissipation and dispersion properties compared to second order finite-volume schemes.

One approach overcome this disadvantage of the DG scheme is to use an adaptive mesh refinement (AMR). In the surrounding of the phase boundary, that is detected using a level-set based indicator, the mesh is refined using a second-order finite volume method, that has the same number of degrees of freedom. In the refined region the gradient is reconstructed using a slope limiter to avoid oscillations next to the phase boundary. This implies that one DG cell is refined into multiple finite-volume cells. At the resulting interface between the polynomial DG cells and the refined finite volume cells a conservative projection/reconstruction method is used to ensure consistency at the interface between refined and polynomial grid cells. This approach is used for the conservation variables of the Navier-Stokes equations as these quantities may be discontinuous across a phase interface. The level-set variable is always treated with DGSEM as for the calculation of the curvature a high order level-set solution is necessary. The input for the level-set, the advection velocity field, is interpolated onto the DG integration points for each Runge-Kutta stage. Similarly, the resulting level-set value is projected onto the finite-volume cells.

The effect of AMR on the approximation of the numerical phase boundary is visualized in figure 2 showing the density iso-contour of the liquid phase. For this study a sixth-order DG scheme (polynomial degree $N = 5$) was used that corresponds to the setting used in the first test case (steady droplet). This AMR approach combines both the high order resolution of a DG scheme as well as the fine resolution of discontinuities of a finite volume scheme. In order to limit the impact of the underlying finite-volume scheme on the global solution, the AMR approach is limited to a small region next to the physical phase boundary.

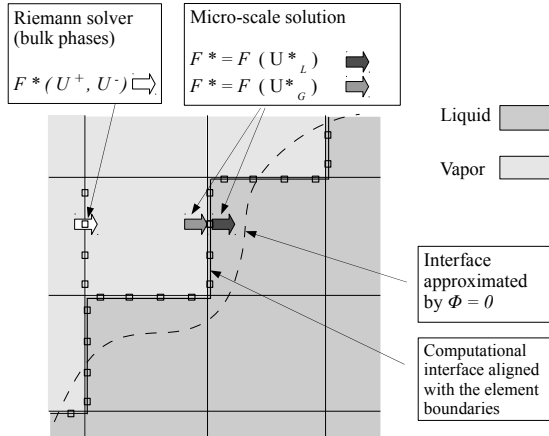


Figure 3: Schematic of a typical setting in the HMM approach for the native DG approach, involving the liquid-vapor interface, approximated by the zero level-set $\Phi = 0$, the computational interface and the different ways to apply the numerical fluxes provided by either a standard Riemann solver (bulk phase) or the micro-scale solver at the computational interface.

2.5 Micro-scale solver

The micro-solver used in this case is an approximate HLLC Riemann solver as proposed by Hu et al. [2]. The Riemann solver is modified to take surface tension into account and is employed at the computational interface. The density discontinuity in the used sharp interface approach across a phase interface is resolved using the wave pattern of contact discontinuity. This is the natural choice to resolve phase discontinuities as primarily the density is discontinuous. In order to include surface tension in this approximate Riemann solver, the pressure can be discontinuous across the phase boundary. The pressure drop magnitude is determined by the Young-Laplace law (1) using the mean curvature of the level-set at the physical phase boundary that is determined in the macro-scale solver (see step 1 of the solution algorithm).

The contact discontinuity is the standard choice to resolve the phase interface as across the contact discontinuity no mass transfer is occurring. Furthermore, this discontinuity represents well the occurrence in multiphase flows as typically only the densities of the different fluids vary by some order of magnitudes. The velocity of contact discontinuity is taken as a model for the propagation speed of the interface s as needed for the level-set transport equation.

3 Transfer of information between macro-scale and micro-scale solver

The transfer of information from the micro- to the macro-solver relies on the numerical fluxes at the computational interface as illustrated in figure 3. In the bulk phases away from the computational interface, the DGSEM incorporates a standard HLLC Riemann solver to obtain the numerical flux \mathbf{F}^* inside the single-phase region. For the element faces that form the computational interface, the micro-scale solver is used instead. Let $\mathbf{U}_L := \mathbf{U}^-$ and $\mathbf{U}_G := \mathbf{U}^+$ be the respective states in the two different phases in some quadrature point. These states are the input for the micro-scale solver (together with the curvature; if surface tension is considered). The micro-scale solver delivers for each quadrature point a liquid state \mathbf{U}_L^* and a gaseous state \mathbf{U}_G^* . The DGSEM now uses the flux evaluations $\mathbf{F}^* = \mathbf{F}(\mathbf{U}_L^*)$ for the computation on the liquid element and $\mathbf{F}^* = \mathbf{F}(\mathbf{U}_G^*)$ for the computation on the gaseous element. Inside the AMR region the numerical fluxes are used on each face of the refined finite-volume cells. This method of calculating two different fluxes for each phase results in a solution where variables such as the density remain discontinuous across the (computational) interface and the typical numerical smearing of discontinuities in numerical schemes is avoided. For piecewise constant approximations the method is similar to the ghostfluid method [3, 12], where two different fluxes are obtained via additional ghost states near the interface.

In this study, we include the effect of surface tension, which necessitates two elements: the first is the evaluation of the local curvature of the interface, the second is the application of the resulting surface force on the flow. In the literature, a common way to do the latter is to replace the surface force by a distribution of a volume source term, e.g. the continuum surface force method of Brackbill and Kothe [13]. In the HMM approach of the present study, the effect of surface tension is entirely handled in the micro-scale solver. This way, the surface tension force is exerted on the macro-scale through the fluxes at the computational interface. Inversely, it is necessary to provide the micro-scale with information on the mean curvature κ , which is obtained from the divergence of the level-set normal:

$$\kappa = \operatorname{div} \left(\frac{\operatorname{grad}(\Phi)}{|\operatorname{grad}(\Phi)|} \right). \quad (11)$$

This quantity is only meaningful at zero level-set which does not always coincide with the computational interface as the numerical interface is only a rough approximation to the physical interface. In case of the native DG approach the curvature value, for each micro-solver, at the physical interface is obtained using a 1D search normal to the cell boundary until the nearest root of the level-set is found. In the AMR case the curvature value can be obtained easily by evaluating the curvature value at the refined grid cells on both sides of the phase boundary.

4 Results

To illustrate the performance of the method, three test cases with increasing complexity are presented. All cases consider three-dimensional, spherical droplets.

In all test cases the complete Navier-Stokes equations are used together with corresponding equations of states. In the gaseous phase the ideal gas law is applied and in the liquid phase the weakly compressible Tait EOS. Due to the absence of a proper micro-scale model for phase change, mass transfer over the phase boundary is not considered. Because of that physical droplet features like evaporation and condensation can not be treated using the present simple micro-scale model.

4.1 Steady droplet with surface tension

The first test is a simulation of a steady-state droplet including a simple surface tension approach. As described in section 2.5 a HLLC micro-scale solver is used at the phase boundary that incorporates a pressure drop depending on the curvature value. The droplet is initialized at a slightly higher pressure than the surrounding gas (see table 1 for a summary of the initial conditions). The resulting pressure difference matches the pressure jump resulting from surface tension at the given droplet diameter, therefore leading to a steady-state condition if the calculation of the curvature and the resulting micro-scale solution are accurate.

The simulation has been conducted over a dimensionless time of $t = 0.3$ representing about 570 iterations. A Weber number based on this time period and the diameter of $d = 0.3$ m is of the order of 10^6 . The cartesian grid is very coarse, consisting only of $15 \times 15 \times 15$ cells, the polynomial degree of the DG scheme has been chosen as $N = 5$. Figure 4 shows pressure information extracted on the mid-plane of the droplet at $t = 0.15$. The jump in the pressure is visible at the cell boundaries near the level-set zero. The constant states on the gaseous side have been perfectly conserved while minor fluctuations have developed on the liquid side. The corresponding result is shown for the case without the use of AMR at the phase boundary and with AMR. The resolution of the physical interface is much better using AMR especially for the here considered high order scheme. In the AMR case minor fluctuations due to the stiff Tait EOS occur next to the interface that might be related to the postprocessing of the results as for visualization the solution is super-sampled.

4.2 Advected droplet with surface tension

The previous steady-state test case is extended in the following way that a global droplet advection velocity in x -direction is added. Similarly to the previous test case a HLLC micro-solver is applied at the phase boundary. All other example parameters remain unchanged including the pressure drop between the droplet and the surrounding air and the calculation of surface tension. The example parameters shown in table 1

Droplet radius	Inner state	Outer state
$r_{\text{ini}} = 0.4$	$\rho = 1000$ $ \mathbf{v} = 0.0$ $p = 1.0$	$\rho = 1.0$ $ \mathbf{v} = 0.0$ $p = 0.996365$
Surface tension coeff.	Tait EOS parameters inner state	Ideal gas EOS parameters outer state
$\sigma = 0.000727$	$\kappa_L = 7.15$, $k_0 = 3310$, $\rho_0 = 1000$, $p_0 = 1.0$	$\kappa = 1.4$

Table 1: Initial conditions of the steady droplet with surface tension.

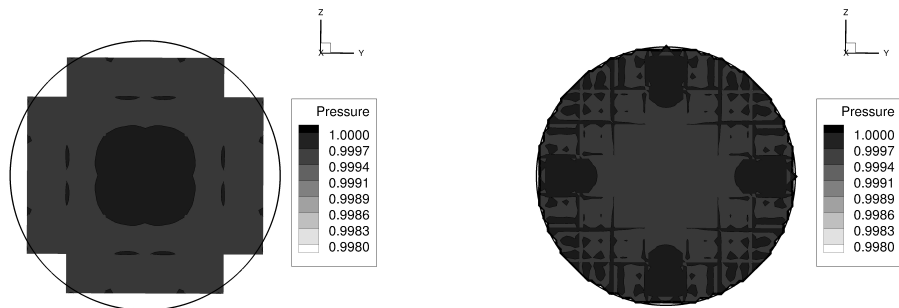


Figure 4: Result of the steady droplet test case with surface tension at $t = 0.15$. The black line visualizes the physical phase boundary (zero level-set). **Left:** Pressure contours on the droplet median plane obtained for the case without AMR. **Right:** Pressure contours on the droplet median plane with the use of AMR at the phase boundary.

apply for this case as well with the exception of the bulk fluid velocity that is set to $\mathbf{v} = (1, 0, 0)^T$. Because of that no steady-state solution is reached but the droplet is advected with the fluid flow in x -direction. The applied surface tension prevents the droplet from dilution during advection.

The simulation has been conducted over a dimensionless time for $t = 0.3$ representing 1120 iterations. A Weber number based on the advection velocity and the droplet diameter of $d = 0.3$ m is of the order of 10^6 . For this simulation a lower polynomial degree ($N = 3$, resulting in a 4th order scheme) was chosen in order to limit the negative effects of the state extrapolation procedure on the solution in case the droplet is convected downstream. A finer cartesian grid with the size of $30 \times 30 \times 30$ grid cells in the corresponding axis directions is chosen. The pressure distribution is presented in Figure 5 at time $t = 0.15$ for both considered configurations. On the left the pressure distribution is shown for the pure DG simulation (without refinement at phase boundaries) and on the right the simulation incorporating AMR.

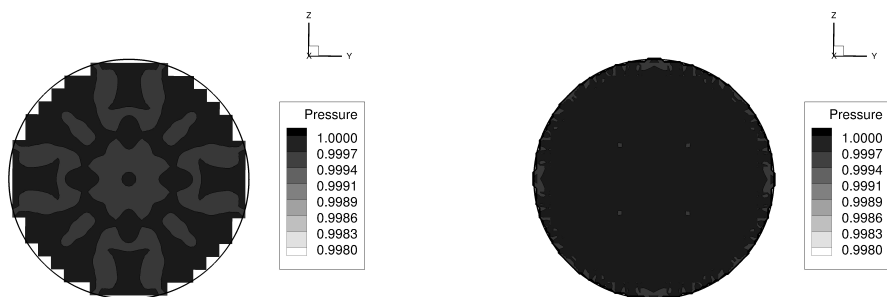


Figure 5: Result of the advection droplet test case with surface tension at $t = 0.15$ resulting in an advected distance of $x_{\text{adv}} = 0.15$. The physical phase boundary (zero level-set) is visualized by the black line. **Left:** Pressure contours on the droplet median plane obtained for the case without AMR. **Right:** Pressure contours for the droplet median plane with the use of AMR at the phase boundary.

Droplet radius	Inner state			Outer state (pre/post-shock)		
$r_{\text{ini}} = 0.00175$	$\rho = 1000$	$ \mathbf{v} = 0.0$	$p = 1.0$	$\rho = 1.0$	$ \mathbf{v} = 0.0$	$p = 1.0$
	EOS parameters inner state			EOS parameters outer state		
	$\kappa_L = 7.15, k_0 = 3310, \rho_0 = 1000, p_0 = 1.0$			$\rho = 1.32575, \mathbf{v} = (0.346215, 0, 0), p = 1.48783$		
				$\kappa = 1.4$		

Table 2: Initial conditions for the droplet interacting with a planar shock wave.

4.3 Shock-droplet interaction

The third test considers a planar shock wave impinging on a spherical droplet. The initial conditions are given in table 2. The fine cartesian grid consists of $50 \times 50 \times 50$ cells while for the coarse grid only $30 \times 30 \times 30$ are used. The polynomial degree is chosen to $N = 2$ and surface tension is not considered. The result is shown in figure 6, showing pressure contours inside the droplet on the median plane as well as outside in the gaseous region for the cases with AMR and without. On top the result for the coarse grid is shown, while below the result on the fine grid is shown. All plots are taken at a simulation time of $t = 1.5 \cdot 10^{-3}$ s.

The shock is partly reflected on the droplet, the other part enters into the liquid. Inside the droplet the shock travels at much higher speed. At the curved surface of the droplet the shock wave is reflected and distorted. The main features of the simulations appear as physical and resemble the (higher resolved but 2D) results shown by Hu et al. [2].

In the simulation without AMR, the coarse staircase pattern of the computational interface appears as visible perturbation in the result that is clearly visible on the coarse grid. While the reflected shock front quickly regains a smooth shape after clearing the angular computational interface, the airflow following the shock leads to unphysical fluctuations when passing over the jagged regions, revealing the limits of the method without the use of AMR.

The use of AMR sufficiently improves the resolution of the computational interface as well as the flow field in the surrounding of the droplet. Thus the previously visible unphysical staircase pattern is significantly reduced at the phase boundary. Even on the coarse grid the staircase pattern is hardly visible. The high pressure region next to the stagnation point on the droplet is clearly visible and not distorted by staircase pattern of the computational interface.

5 Conclusion and Future Work

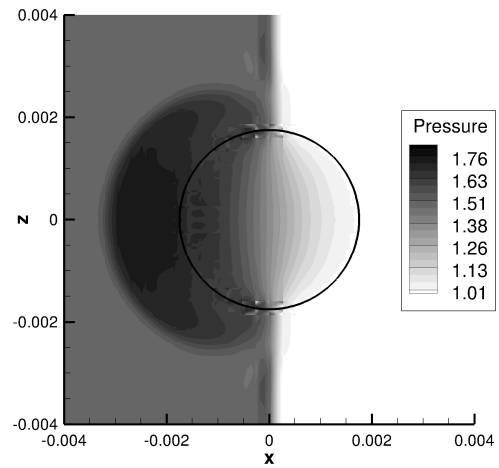
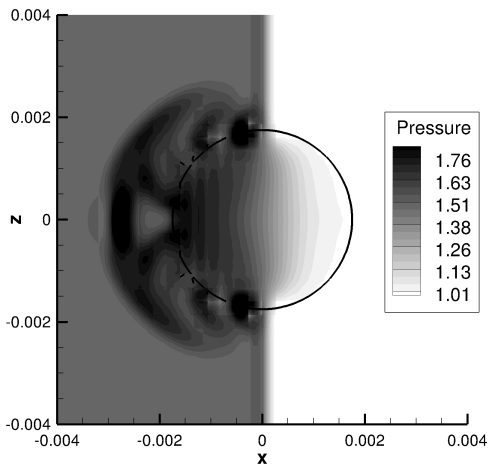
A numerical method for compressible two-phase flows using a sharp interface method is described and applied in 3D. The present numerical approach allows for a high order of accuracy as well as efficient calculations. The high order is of advantage for the resolution of the interface as well as its curvature. Basic ideas are taken from the popular ghost-fluid approach and are adapted for the DG framework. The numerical fluxes at the computational interface are obtained correctly using the solution of two-phase Riemann problems. It is shown that the resolution of the numerical interface can be considerably improved through the use of adaptive mesh refinement near the phase boundary.

The presented 3D test cases show the capabilities of the used solution algorithm for compressible fluids and the results show good agreement to reference solutions.

6 Acknowledgements

The authors gratefully acknowledge the support by the German Research Foundation (DFG) through SFB TRR 75 ‘‘Droplet dynamics under extreme ambient conditions’’ as well as the Carl Zeiss Foundation.

Coarse grid:



Fine grid:

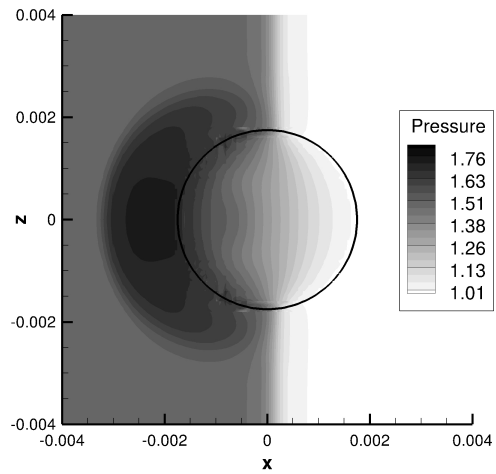
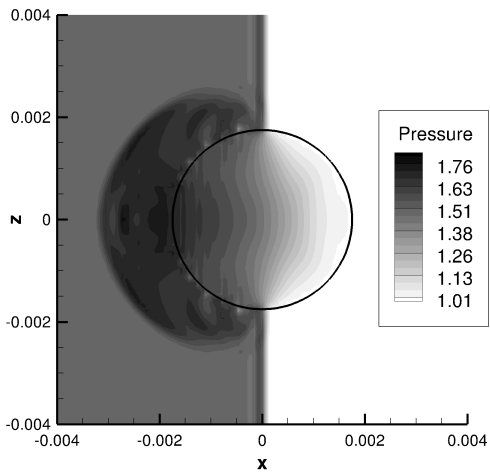


Figure 6: Result of a droplet interacting with a planar shock at $t = 1.5 \cdot 10^{-3}$ s. On top the result for the coarse grid ($30 \times 30 \times 30$ cells) is shown and on the bottom the fine grid ($50 \times 50 \times 50$ cells). **Left:** pressure contours on the droplet median plane without AMR. **Right:** pressure contours on the droplet median plane with the use of AMR at the phase boundary.

References

- [1] Christian Merkle and Christian Rohde. The sharp-interface approach for fluids with phase change: Riemann problems and ghost fluid techniques. *ESAIM: Mathematical Modelling and Numerical Analysis*, 41(06):1089–1123, 2007.
- [2] X. Y. Hu, N. A. Adams, and G. Iaccarino. On the HLLC Riemann solver for interface interaction in compressible multi-fluid flow. *J. Comput. Phys.*, 228(17):6572–6589, 2009.
- [3] R. P. Fedkiw, T. Aslam, B. Merriman, and S. Osher. A non-oscillatory Eulerian approach to interfaces in multimaterial flows (the ghost fluid method). *J. Comput. Phys.*, 152(2):457–492, 1999.
- [4] T. G. Liu, B. C. Khoo, and K. S. Yeo. Ghost fluid method for strong shock impacting on material interface. *J. Comput. Phys.*, 190(2):651–681, 2003.
- [5] A. Ferrari, C.-D. Munz, and B. Weigand. A High Order Sharp-Interface Method with Local Time Stepping for Compressible Multiphase Flows. *Commun. Comput. Phys.*, 9:205–230, 2010.
- [6] David A. Kopriva and Gregor Gassner. On the Quadrature and Weak Form Choices in Collocation Type Discontinuous Galerkin Spectral Element Methods. *J. Sci. Comput.*, 44:136–155, 2010.
- [7] F. Jaegle and V. Schleper. Exact and approximate Riemann solvers at phase boundaries. *Preprint 2012*, 2012.
- [8] D. A. Kopriva. Spectral Element Methods. *Implementing Spectral Methods for Partial Differential Equations*, pages 293–354, 2009.
- [9] F. Jaegle, C. Zeiler, and C. Rohde. A multi-scale algorithm for compressible liquid-vapour flow with surface tension. *Preprint 2012*.
- [10] Mark Sussman, Peter Smereka, and Stanley Osher. A Level Set Approach for Computing Solutions to Incompressible Two-Phase Flow. *Journal of Computational Physics*, 114(1):146–159, 1994.
- [11] Jue Yan and Stanley Osher. A local discontinuous Galerkin method for directly solving Hamilton-Jacobi equations. *J. Comput. Physics*, 230(1):232–244, 2011.
- [12] C. Merkle and C. Rohde. The sharp-interface approach for fluids with phase change: Riemann problems and ghost fluid techniques. *M2AN Math. Model. Numer. Anal.*, 41(6):1089–1123, 2007.
- [13] J. U. Brackbill, D. B. Kothe, and C. Zemach. A continuum method for modeling surface tension. *Journal of computational physics*, 100(2):335–354, 1992.